Figures and figure supplements

ROM1 is redundant to PRPH2 as a molecular building block of photoreceptor disc rims

Tylor R Lewis *et al*.

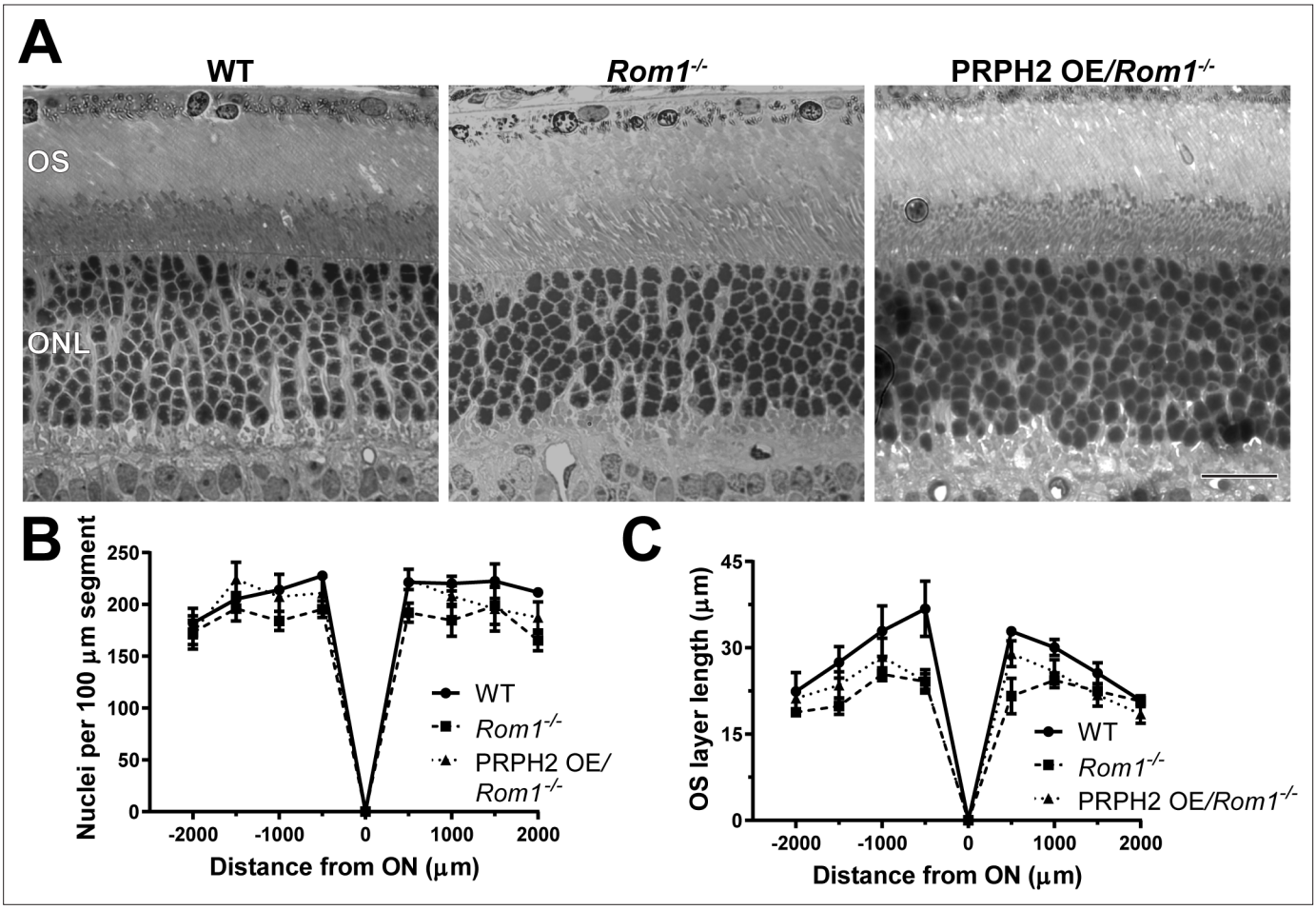

Figure 1. Light microscopy of retinas from WT, *Rom1*$^{-/-}$ and PRPH2 OE/*Rom1*$^{-/-}$ mice. (**A**) Representative light microscopy images of WT, *Rom1*$^{-/-}$ and PRPH2 OE/*Rom1*$^{-/-}$ retinas analyzed at P30. OS: outer segment; ONL: outer nuclear layer. Scale bar: 20 µm. (**B**) Quantification of the number of photoreceptor nuclei in a 100 µm segment of the retina at 500 µm increments away from the optic nerve (ON). Three retinas were analyzed for each genotype. Two-way ANOVA revealed statistically significant differences in the nuclear counts across genotypes (p=0.0002). Sidak's multiple comparisons post-hoc test revealed statistically significant differences between the total nuclear count between WT and *Rom1*$^{-/-}$ retinas (p=0.0001) and between *Rom1*$^{-/-}$ and PRPH2 OE/*Rom1*$^{-/-}$ retinas (p=0.0148), but not between WT and PRPH2 OE/*Rom1*$^{-/-}$ retinas (p=0.3564). (**C**) Quantification of the outer segment (OS) layer length at 500 µm increments away from the optic nerve. Three retinas were analyzed for each genotype. Two-way ANOVA revealed statistically significant differences in the OS layer lengths across genotypes (p<0.0001). Sidak's multiple comparisons post-hoc test revealed statistically significant differences for the OS layer length between WT and *Rom1*$^{-/-}$ retinas (p<0.0001) and between WT and PRPH2 OE/*Rom1*$^{-/-}$ retinas (p=0.0006), but not between *Rom1*$^{-/-}$ and PRPH2 OE/*Rom1*$^{-/-}$ retinas (p=0.2924).

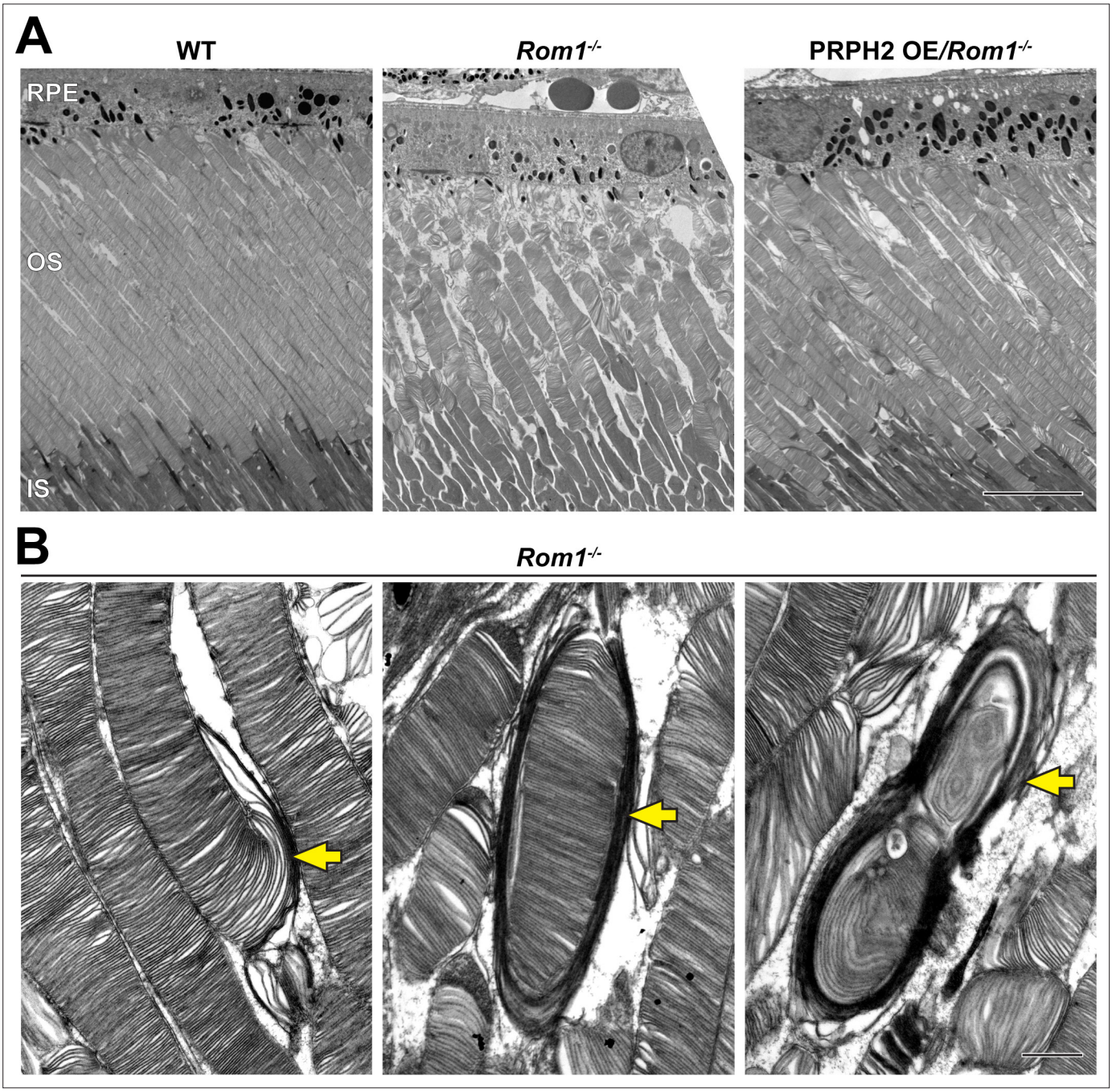

Figure 2. Ultrastructural analysis of retinas and rod outer segments from WT, *Rom1*$^{-/-}$ and PRPH2 OE/*Rom1*$^{-/-}$ mice. (**A**) Representative low magnification TEM images of WT, *Rom1*$^{-/-}$ and PRPH2 OE/*Rom1*$^{-/-}$ retinas analyzed at P30. RPE: retinal pigment epithelium; OS: outer segment; IS: inner segment. Scale bar: 10 μm. (**B**) Representative high-magnification TEM images of *Rom1*$^{-/-}$ outer segments. Yellow arrows indicate outer segment structural defects that range from slightly overgrown open discs to membranous whorls. Scale bar: 1 μm.

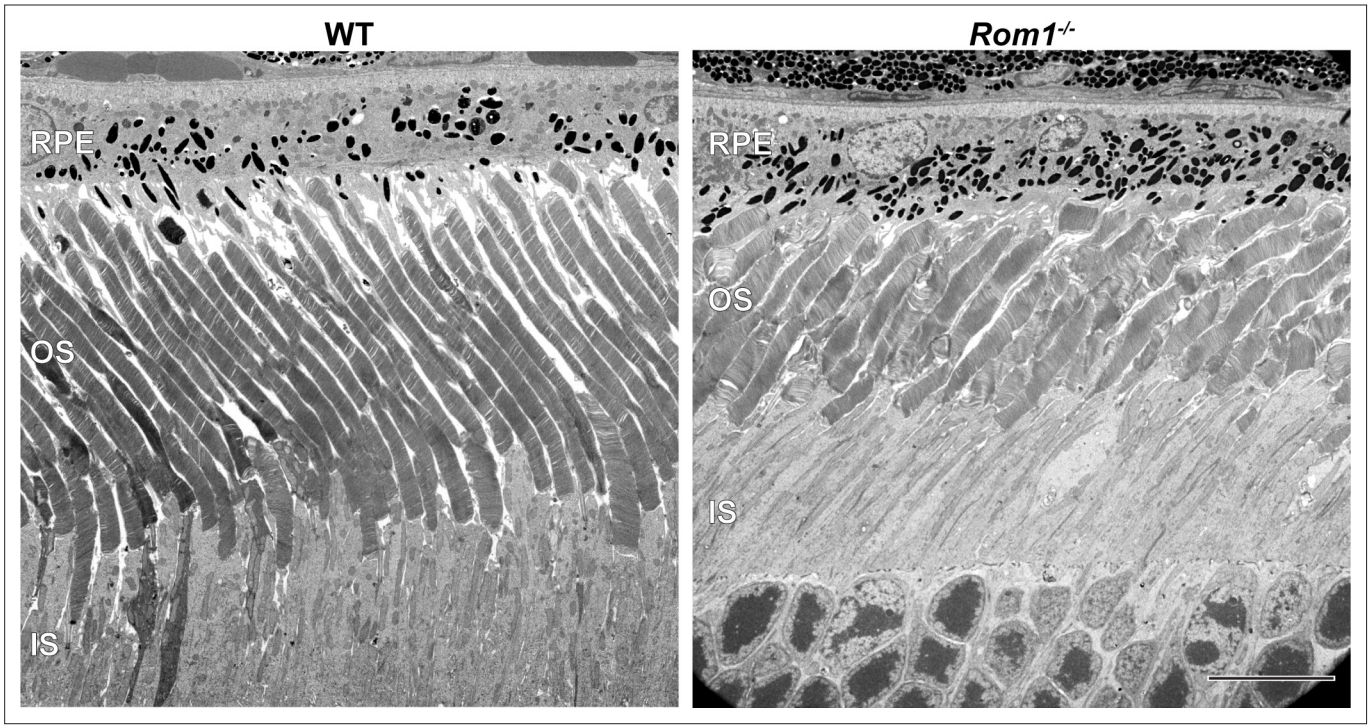

Figure 2—figure supplement 1. Ultrastructural analysis of WT and *Rom1*$^{-/-}$ retinas. Representative low magnification TEM images of WT and *Rom1*$^{-/-}$ retinas contrasted with the conventionally used osmium tetroxide. RPE: retinal pigment epithelium; OS: outer segment; IS: inner segment. Scale bar: 10 μm.

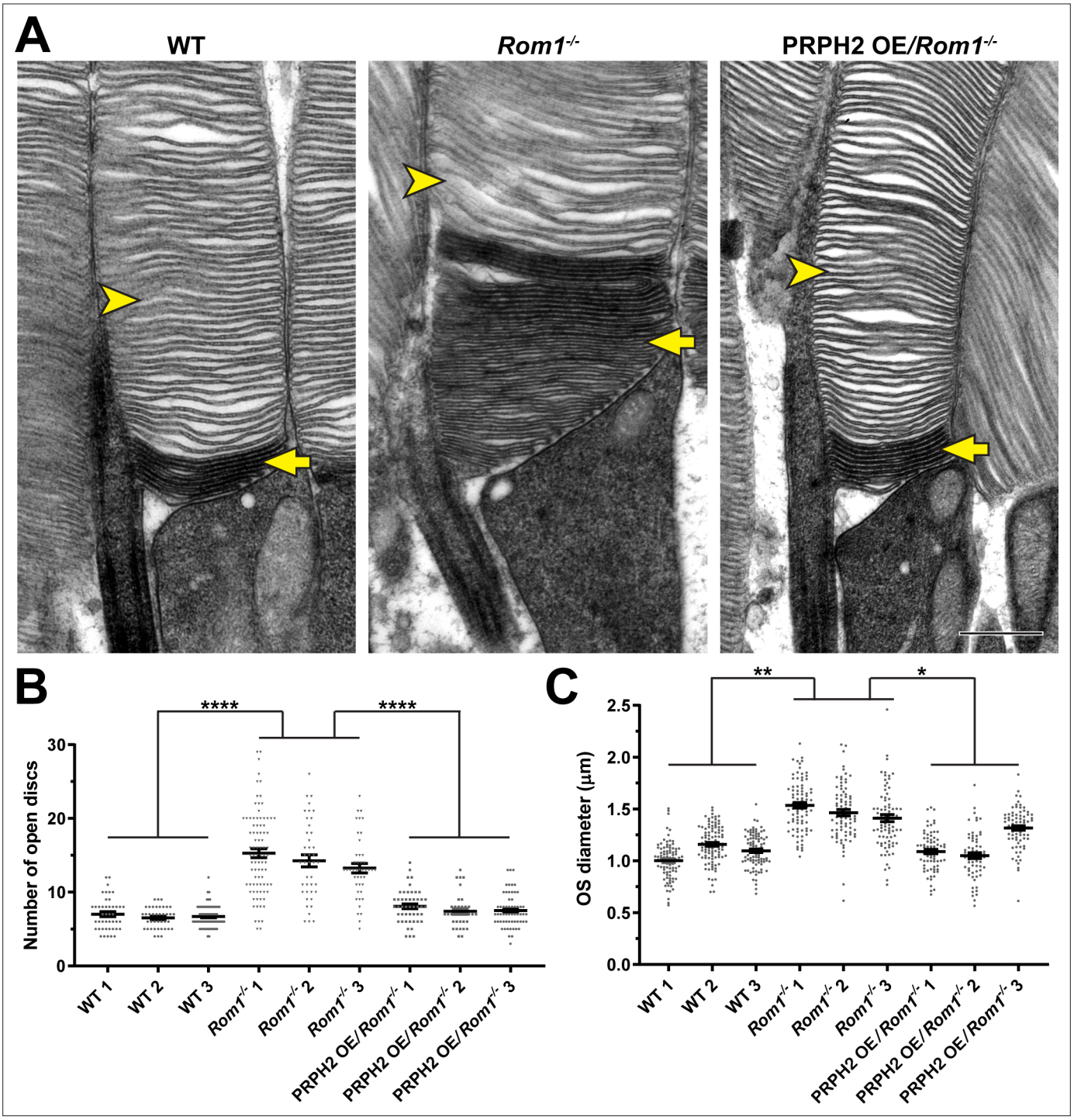

Figure 3. Analysis of disc enclosure in rod outer segments of WT, *Rom1*$^{-/-}$ and PRPH2 OE/*Rom1*$^{-/-}$ mice. (**A**) Representative high magnification TEM images of tannic acid/uranyl acetate-stained retinas of WT, *Rom1*$^{-/-}$ and PRPH2 OE/*Rom1*$^{-/-}$ mice analyzed at P30. This approach stains newly forming 'open' discs more intensely than mature enclosed discs. Yellow arrows point to darkly stained, unenclosed discs; yellow arrowheads point to lightly stained, enclosed discs. Scale bar: 0.5 µm. (**B**) Quantification of the number of darkly stained open discs at the rod outer segment base. Each data point represents a single outer segment. For each genotype, three retinas were analyzed with at least 35 outer segments analyzed per retina. Data were plotted with samples separated, while statistical analysis was performed on the averages within each retina (n=3 for each genotype). One-way ANOVA revealed statistically significant differences in the number of open discs across genotypes ($p<0.0001$). Tukey's multiple comparisons post-hoc test revealed statistically significant differences in the number of open discs between WT and *Rom1*$^{-/-}$ ($p<0.0001$) and *Rom1*$^{-/-}$ and PRPH2 OE/*Rom1*$^{-/-}$ ($p<0.0001$) mice, but not between WT and PRPH2 OE/*Rom1*$^{-/-}$ mice ($p=0.2686$). (**C**) Quantification of the outer segment (OS) diameter. For each genotype, three retinas were analyzed with at least 66 outer segments analyzed per retina. One-way ANOVA revealed statistically significant differences

Figure 3 continued on next page

Figure 3 continued

in the OS diameters across genotypes (p=0.0074). Tukey's multiple comparisons post-hoc test revealed statistically significant differences in the OS diameters between WT and *Rom1*$^{-/-}$ (p=0.0083) and *Rom1*$^{-/-}$ and PRPH2 OE/*Rom1*$^{-/-}$ (p=0.0197) mice, but not between WT and PRPH2 OE/*Rom1*$^{-/-}$ mice (p=0.7198). Note that these diameters were measured in longitudinal sections, in which outer segment are not always sectioned across their widest part; therefore, these values are likely under-representations of the true OS diameters. However, this does not affect the comparison across genotypes.

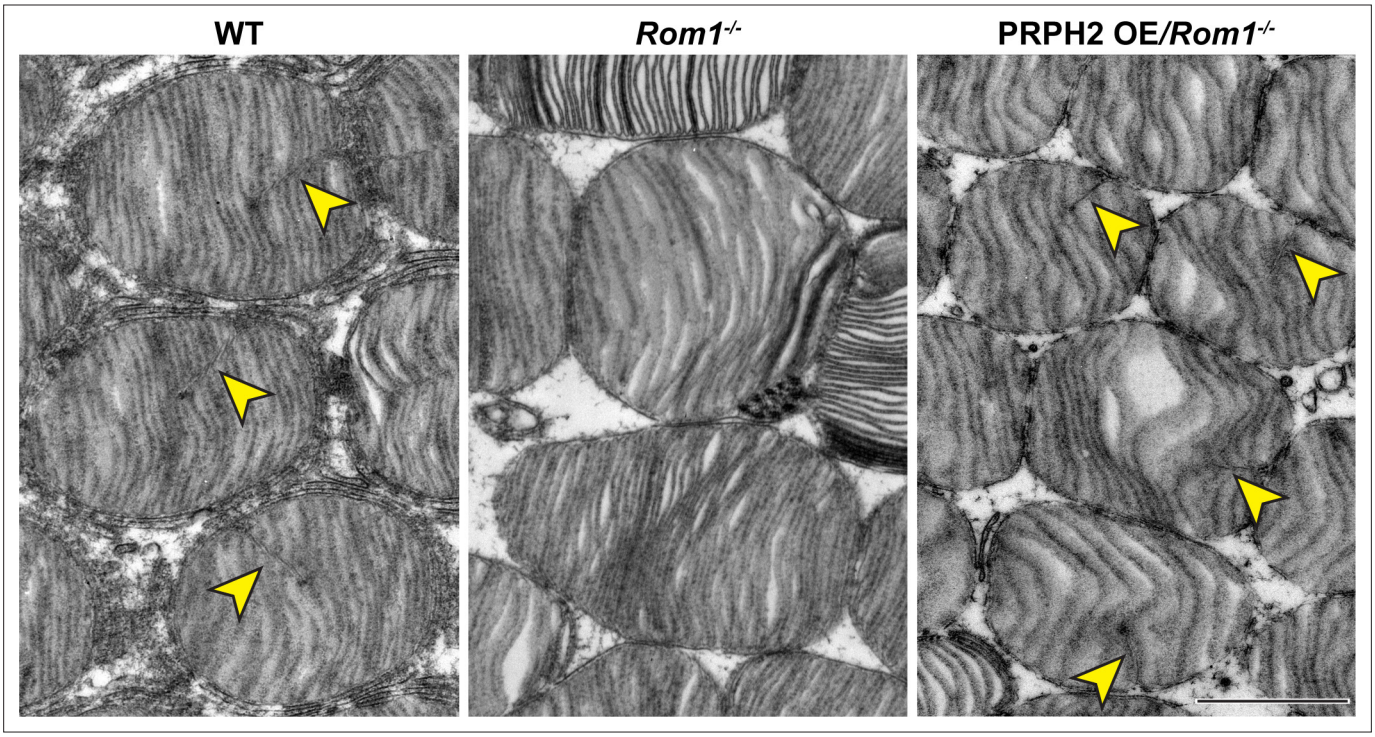

Figure 4. Ultrastructural analysis of disc incisures in WT, *Rom1*$^{-/-}$ and PRPH2 OE/*Rom1*$^{-/-}$ mice. Representative TEM images of retinas, tangentially sectioned through the outer segment layer, from WT, *Rom1*$^{-/-}$ and PRPH2 OE/*Rom1*$^{-/-}$ mice analyzed at P30. Yellow arrowheads indicate incisures observed in WT and PRPH2 OE/*Rom1*$^{-/-}$ discs, but not *Rom1*$^{-/-}$ discs. Scale bar: 1 μm.

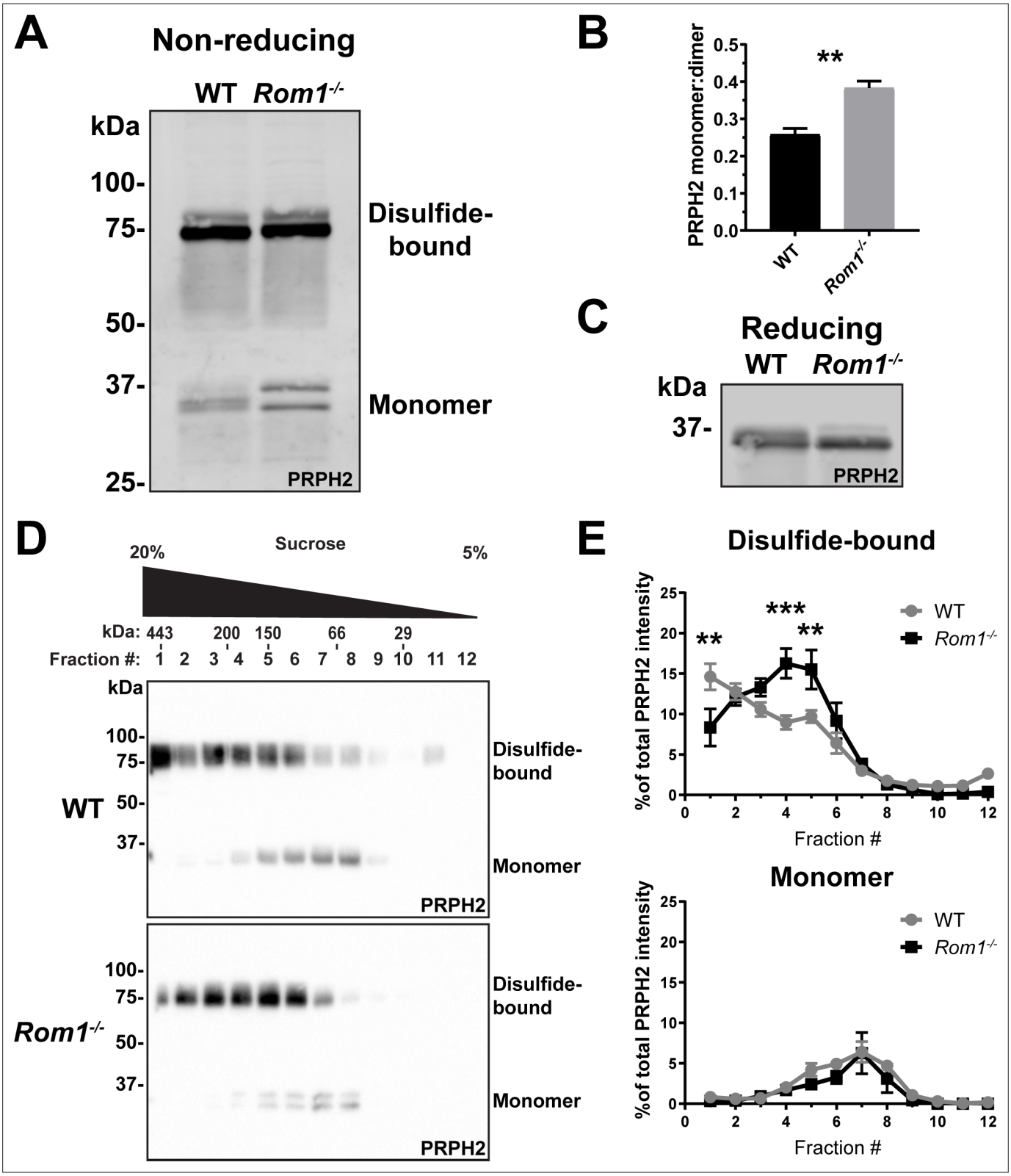

Figure 5. Loss of ROM1 alters the oligomerization status of PRPH2. (**A**) Western blot probed for PRPH2 after protein separation by SDS-PAGE under non-reducing conditions. Each sample contained 10 µg of lysate obtained from eyecups of WT or *Rom1*$^{-/-}$ mice at P30. Under these conditions, PRPH2 runs as disulfide-bound dimers (~75 kDa) and monomers (~37 kDa). The monomer band of PRPH2 runs as a doublet in *Rom1*$^{-/-}$ but not WT eyecups. (**B**) Quantification of the ratio between monomer and disulfide-bound (dimer) bands of PRPH2 was performed using densitometry of three independent

Figure 5 continued on next page

Figure 5 continued

lysates. For the doublet of monomer bands in *Rom1*$^{-/-}$ lysates, both bands were used for quantification. Unpaired t-test revealed a statistically significant difference in the PRPH2 monomer:dimer ratio between WT and *Rom1*$^{-/-}$ retinas (p=0.0071). (**C**) Western blot probed for PRPH2 after protein separation by SDS-PAGE under reducing conditions. Each sample contained 10 µg of lysate obtained from eyecups of WT or *Rom1*$^{-/-}$ mice. (**D**) Lysates obtained under non-reducing conditions from eyecups of WT and *Rom1*$^{-/-}$ mice were subjected to velocity sedimentation on 5–20% sucrose gradients. Twelve fractions were collected with fraction #1 corresponding to 20% sucrose and fraction #12 to 5% sucrose. Proteins from each fraction were subjected to non-reducing SDS-PAGE and Western blotting for PRPH2. The distribution of molecular mass standards across fraction, as determined in ***Chakraborty et al., 2008***, is shown above the panels. (**E**) Quantification of both the monomeric and disulfide-bound bands of PRPH2 in each fraction was performed using densitometry of at least four independent samples and normalized to the total PRPH2 content across all fractions. Two-way ANOVA revealed statistically significant differences in the PRPH2 content across genotypes and fractions (p<0.0001 for disulfide-bound, p=0.9489 for monomer). Sidak's multiple comparisons post-hoc test revealed statistically significant differences between genotypes for the disulfide-bound form in fractions #1 (p=0.0022), #4 (p=0.0002), and #5 (p=0.0061).

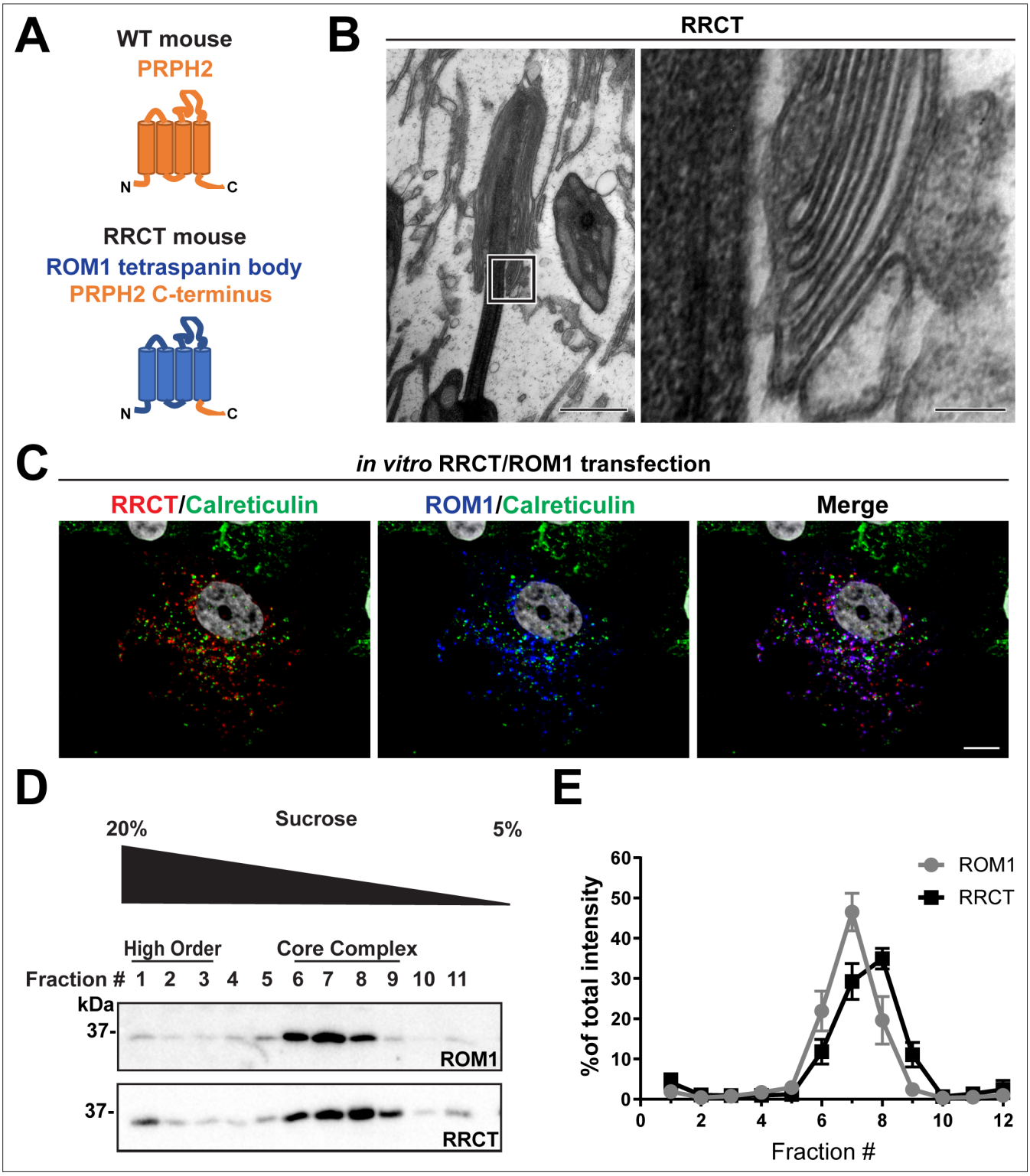

Figure 6. The tetraspanin body of PRPH2 can be replaced by that of ROM1 in disc rim formation. (**A**) Cartoon schematic of the RRCT chimeric tetraspanin protein. In the RRCT mouse, the *Prph2* gene has a knockin mutation that replaces it with a DNA sequence encoding a chimeric protein consisting of the tetraspanin body of ROM1 while retaining the C-terminal tail of PRPH2 that is essential for disc formation. (**B**) Representative TEM images of homozygous RRCT mice analyzed at P30. The boxed inset (left) is shown at a higher magnification (right) that reveals the presence of disc rims. Scale bars: 1 µm (left); 0.1 µm (right). (**C**) Immunofluorescent images of COS-7 cells co-transfected with RRCT-FLAG and ROM1 constructs. Cells were stained with antibodies against RRCT (red), ROM1 (blue) and calreticulin (green) to label ER membranes. Nuclei were counterstained with DAPI (grey). Scale bar: 10 µm. (**D**) Lysates obtained under non-reducing conditions from COS-7 cells co-transfected with RRCT-FLAG and ROM1 constructs

Figure 6 continued on next page

Figure 6 continued

were subjected to velocity sedimentation on 5–20% sucrose gradients. Twelve fractions were collected with fraction #1 corresponding to 20% sucrose and fraction #12 to 5% sucrose. Proteins from each fraction were subjected to reducing SDS-PAGE and Western blotting for ROM1 and RRCT. (**E**) Quantification of ROM1 and RRCT in each fraction was performed using densitometry of three independent lysates and normalized to the total content across all fractions.

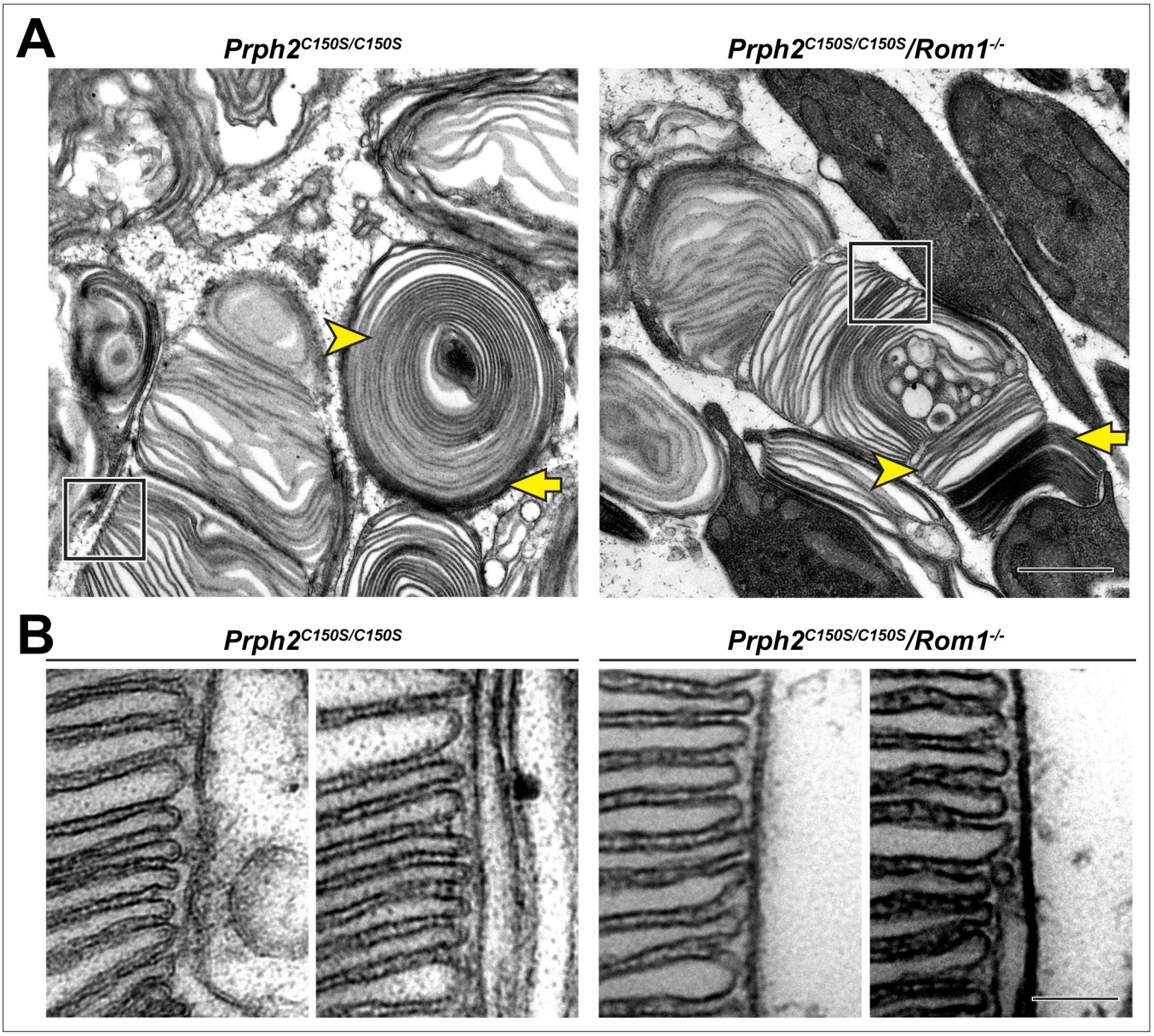

Figure 7. Disc rims can be formed in the absence of intermolecular disulfide bonds between PRPH2 and ROM1. (**A**) Representative TEM images of tannic acid/uranyl acetate-stained retinas of *Prph2*$^{C150S/C150S}$ and compound *Prph2*$^{C150S/C150S}$/*Rom1*$^{-/-}$ mice analyzed at P30. Photoreceptor outer segments of each mouse have severely perturbed outer segment structure. Yet, disc enclosure is not completely prevented as there are both darkly-stained, 'open' discs (yellow arrows) and lightly-stained, 'enclosed' discs (yellow arrowheads) in each genotype. The boxed region of each image depicts an area in which disc stacking appears relatively normal and permits the analysis of disc rim structure. Scale bar: 1 µm. (**B**) Higher magnification images of the regions in which disc stacking appears normal in both *Prph2*$^{C150S/C150S}$ and *Prph2*$^{C150S/C150S}$/*Rom1*$^{-/-}$ mice. Disc rims are formed in each genotype. Scale bar: 0.1 µm.